J. Am. Soc. Mass Spectrom. (2013) 24:1477–1488
DOI: 10.1007/s13361-013-0699-5

RESEARCH ARTICLE

Color Matters—Material Ejection and Ion Yields in UV-MALDI Mass Spectrometry as a Function of Laser Wavelength and Laser Fluence

Jens Soltwisch, Thorsten W. Jaskolla, Klaus Dreisewerd

Institute for Hygiene, Westfälische Wilhelms-Universität Münster, 48149 Münster, Germany

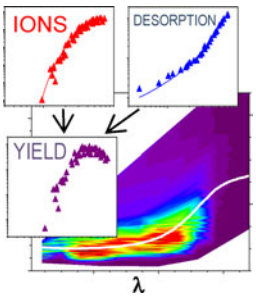

Abstract. The success of matrix-assisted laser desorption/ionization mass spectrometry (MALDI-MS) as a widely employed analytical tool in the biomolecular sciences builds strongly on an effective laser–material interaction that is resulting in a soft co-desorption and ionization of matrix and imbedded biomolecules. To obtain a maximized ion yield for the analyte(s) of interest, in general both wavelength and fluence need to be tuned to match the specific optical absorption profile of the used matrix. However, commonly only lasers with fixed emission wavelengths of either 337 or 355 nm are used for MALDI-MS. Here, we employed a wavelength-tunable dye laser and recorded both the neutral material ejection and the MS ion data in a wide wavelength and fluence range between 280 and 377.5 nm. α-Cyano-4-hydroxycinnamic acid (HCCA), 4-chloro-α-cyanocinnamic acid (ClCCA), α-cyano-2,4-difluorocinnamic acid (DiFCCA), and 2,5-dihydroxybenzoic acid (DHB) were investigated as matrices, and several peptides as analytes. Recording of the material ejection was achieved by adopting a photoacoustic approach. Relative ion yields were derived by division of photoacoustic and ion signals. In this way, distinct wavelength/fluence regions can be identified for which maximum ion yields were obtained. For the tested matrices, optimal results were achieved for wavelengths corresponding to areas of high optical absorption of the respective matrix and at fluences about a factor of 2–3 above the matrix- and wavelength-dependent ion detection threshold fluences. The material ejection as probed by the photoacoustic method is excellently fitted by the quasithermal model, while a sigmoidal function allows for an empirical description of the ion signal–fluence relationship.

Key words: MALDI-MS, Matrix, Laser wavelength, Material ejection, Photoacoustic, Ion yield, Dye laser, ClCCA, DiFCCA

Received: 15 March 2013/Revised: 24 June 2013/Accepted: 1 July 2013/Published online: 14 August 2013

Introduction

A sensitive analysis of large, thermally labile biomolecules by matrix-assisted laser desorption/ionization mass spectrometry (MALDI-MS) depends strongly on the effective interplay between the optical properties of the employed matrix and those of the laser light. Although both the excitation wavelength and laser fluence (laser pulse energy per irradiated area) should generally be tuned to achieve a maximum analytical sensitivity [1–4], in practical terms only the second parameter is normally available. Either N_2 or frequency-tripled Nd:YAG lasers, emitting at fixed wavelengths of 337 and 355 nm, respectively, are commonly utilized for UV-MALDI-MS. Consequently, matrices have to be chosen from a limited group of compounds that exhibit a sufficient optical absorption at these wavelengths. Another parameter that crucially determines the analytical sensitivity is the ion yield (i.e., the fraction of detected molecular analyte ions relative to the overall number of consumed analyte molecules). Several of the physicochemical properties of the matrix (e.g., optical absorption coefficient, crystallization behavior, proton affinity) and those of the laser light (e.g., wavelength, pulse duration, fluence, beam profile) are key factors to achieve a high analytical sensitivity. A high ion yield is particularly pivotal when only a limited amount of

Electronic supplementary material The online version of this article (doi:10.1007/s13361-013-0699-5) contains supplementary material, which is available to authorized users.

Correspondence to: Klaus Dreisewerd; *e-mail:* dreisew@uni-muenster.de

sample is available, as for instance in MALDI MS imaging (MSI) applications. In contrast, high ion signals per laser pulse may eventually also be achieved when the ion yield is relatively low, as long as enough material can be sampled and analyte ion signals increase stronger with the number of laser pulses than the background noise.

In a study in which a wavelength-tunable dye laser was employed we recently investigated the MALDI-relevant wavelength region between 280 and 355 nm and recorded the signal intensities of analyte and matrix ions as a function of wavelength and laser fluence. Two of the most common MALDI matrices, α-cyano-4-hydroxycinnamic acid (HCCA) and 2,5-dihydroxybenzoic acid (DHB), as well as a selection of halogenated α-cyanocinnamic acid (CCA)-derivatives with blue-shifted absorption profiles, were investigated [4]. In a follow-up study, in which MALDI-MSI conditions were approximated, we furthermore determined the maximum signal intensities achievable from a single sample position and for selected matrix/wavelength-combinations [5]. Based on the results of these works, as well as of some others in which distinct wavelengths were previously compared [6–9], it can be concluded that in typical MALDI-MS and MALDI-MSI applications the highest analytical sensitivities should generally be obtained for laser wavelengths near the individual solid-state absorption maxima of the matrices. With respect to the laser fluence, the results of both our study [5] and those of a preceding one by Qiao et al. [10]—the latter was performed in a similar way but utilizing only two fixed wavelengths of 337 and 355 nm—suggest that an optimal sensitivity may typically be achieved if a laser energy exceeding the ion detection threshold 2- to 3-fold is applied, in line with the general empirical experience made by MALDI practitioners. Together, the investigations suggest that applying higher fluences still generally increases the analyte ion signal per laser pulse, but at the cost of a more extensive removal of material, such that the ion yield is, in fact, diminishing.

MALDI ion yields are generally estimated to fall within a range of 10^{-4} to 10^{-3} even under optimal conditions [3, 11, 12]. Therefore, the vast majority of particles is ejected in the form of (or immediately recombines to) neutral molecules rather than ions. Consequently, a comprehensive evaluation of the wavelength- and fluence-dependent analyte ion yields requires recording the overall material ejection in parallel with the ion data. Because not much more than a few monolayers of material are ejected under optimal MALDI conditions [3], the determination of absolute amounts of material ablated per laser pulse is not straightforward. However, relative neutral yields can be recorded as a function of laser fluence by using post-ionization [13, 14] or optical detection methods, such as time-resolved fast-flash imaging [14]. Approaches using quartz microbalances [15, 16] and photoacoustic methods have also been utilized. The latter build on the measurement of the pressure wave generated by the ablated material [14, 17]. Assuming that the center of mass velocity of the ablation plume exhibits only a weak dependence on the laser fluence, the compressive amplitude of the pressure wave becomes a direct measure for the amount of ejected material [18]. Two different detection geometries can be applied. Adopting a rear-side detection scheme, the recoil pressure wave propagating through the MALDI sample has been recorded with a piezoelectric sensor on which the samples were prepared [14]. This detection scheme has the advantage that all of the ejected material is contributing equally to the compressive signal, regardless of whether the material is ejected primarily in molecular form and small clusters (desorption) or as larger particles (ablation). However, a disadvantage is that only liquid MALDI samples can be analyzed accurately because of the extensive scattering of the pressure wave in multi-boundary crystallite samples. If a buffer gas is present in front of the MALDI sample, the pressure wave generated by the ejected material can also be picked up at some distance in front of the sample, for example with a sensitive microphone [17]. The advantage of this front-side detection scheme is that both liquid and solid samples can be analyzed equally well. In contrast to rear-side detection, the generated photoacoustic transient will, however, generally depend stronger on the composition of the MALDI plume (i.e., the ratio of molecular species versus clusters and larger particles). It must be assumed that molecular desorption will generally produce a stronger response because of the larger density gradient experienced by these particles upon the phase transition. So far, the overall material ejection in MALDI has only been investigated at single excitation wavelengths.

In addition to the experimental works, theoretical concepts were also applied to simulate the material disintegration and plume dynamics under approximated MALDI conditions [19–23], as well as to predict the MALDI ion yields [24]. Owing to the complex convoluted ionization mechanisms that comprise laser material interaction, solid state effects, desorption, and gas phase processes, a mathematical treatment of the MALDI ion signal intensities and of ion yields is substantially more difficult than that of the overall material ejection (being dominated by the neutral fraction). Only more recently were approaches applied in which the MALDI sample and ablation plume is treated as a reaction vessel. This way the MALDI process can be simulated by numerically integrating differential rate equations for the various physical and chemical processes to give the final ion populations that can be observed as a mass spectrum [21, 25–27]. These methods were, furthermore, combined and amended by molecular dynamics (MD) simulations [23]. A notable outcome of these combined studies is that the relative low ion yields of 10^{-4} to 10^{-3} are largely caused by extensive recombination processes within the excited but not yet ejected material.

With respect to the fluence, in the MALDI-typical range moderately above the ion detection threshold, the overall material ejection generally shows a weaker increase with the laser fluence than the ion data [3]. The exact mechanisms that underlie the material ejection and the generation of gaseous ions in MALDI depend on both the specific irradiation conditions and the matrix properties [3, 21].

Consequently, quite different dependencies of the particle and ion abundances on laser fluence have been found when different matrix/laser systems were investigated [10, 13–15, 28–35]. Within the MALDI-relevant fluence range, molecular desorption is generally governed by a quasithermal dependence of the ejection yield on the fluence (i.e., the amount of material ejected in molecular form is essentially determined by the peak temperature reached in uppermost matrix layers [36]). If overheating of the matrix material at higher energy densities occurs, phase explosion phenomena coming along with the ejection of larger particulates form additional pathways [3, 19]. Under exceedingly high laser fluences and/or stress confinement conditions, spallation of larger particles may also occur [37, 38]. However, classic stress confinement conditions are generally not achieved under typical UV-MALDI conditions with ns-pulsed lasers. For the most typical MALDI systems, ionization seems to occur throughout the whole fluence range in which neutral desorption takes place, albeit the ionization rates can become exceedingly low at the low fluence side, such that an apparent "ion detection threshold" is usually noted [34].

Here we adapted the front-side photoacoustic approach of Heise and Yeung [17] and recorded the overall particle yield as a function of laser fluence and excitation wavelengths between 280 and 377.5 nm. A set of four matrices was investigated. These comprise two of the most commonly used MALDI matrices, DHB and HCCA, as well as the two recently introduced CCA derivatives, 4-chloro-α-cyanocinnamic acid (ClCCA) [39] and α-cyano-2,4-difluorocinnamic acid (DiFCCA) [40]. Compared with standard HCCA, these halogenated matrices exhibit reduced proton affinities, which enhance proton transfer reactions from matrix ions to analyte molecules but, because of the incorporation of strongly electron-withdrawing substituents, this substitution is accompanied by blue-shifted optical absorption profiles. The experiments were designed to allow for a direct comparison with the mass spectrometric data acquired in parallel for the same set of matrices, laser wavelengths, and fluence ranges. By dividing the two data sets, relative ion yields were derived. In contrast to our previous study [4], a slightly larger increment of 7.5 nm (instead of 5 nm) was applied for the wavelength scan while the MALDI-relevant low to intermediate fluence range was covered by a larger number of fluence points and the wavelength limit was also extended from 355 to 377.5 nm. Both enabled a closer comparison with model assumptions.

Experimental

Materials

ClCCA and DiFCCA were synthesized and purified according to [39]. Water was purified by a Synergy Ultrapure Water System (Millipore, Schwalbach, Germany). All other chemicals and solvents were from Sigma-Aldrich (Schnellendorf, Germany). DHB was of >99% purity and used as purchased. HCCA was initially of >98% purity and purified by repeated recrystallization before use.

Sample Preparation

Four peptides (angiotensin II, MW 1045.534 g/mol; substance P, MW 1346.728 g/mol; neurotensin, MW 1671.910 g/mol; renin substrate, MW 1757.925 g/mol; all MW values refer to the neutral monoisotopic species) were used as analyte mix. The analytes were diluted to 2.5 μM per compound in 30% acetonitrile/0.1% trifluoroacetic acid (vol/vol). For the mass spectrometric measurements, the matrices were used as 10 mM (HCCA) or 2 mM (ClCCA and DiFCCA) solutions in 70% acetonitrile (vol/vol) or as 65 mM aqueous solution in the case of DHB. 22.5 μL matrix and 2 μL analyte solution were mixed and 2 μL of the resulting mixture, containing 400 pmol of each peptide, were deposited on a stainless steel target and dried under a gentle stream of air at room temperature. Average crystal sizes were about 5 to 50 μm for the CCA-derivatives and 50 to 200 μm for the DHB preparations. For the photoacoustic measurements, 5 μL-volumes of saturated matrix solutions in acetone were applied to calcium fluoride (CaF_2) sample plates of 2 mm thickness and allowed to dry under continuous gentle rocking motion of the plate. Typically, the matrix application step was repeated 4 to 5 times until a complete coverage of the sample plates with a homogeneous microcrystalline matrix layer was achieved, as verified with a microscope. Generation (and maintenance during laser irradiation) of a complete coverage of the substrate is a prerequisite for reproducible photoacoustic experiments. Due to the different solvent systems, mean crystal diameters were smaller than for the MS experiments and ranged from 1 to 5 μm for all investigated matrices.

Spectrophotometry

Solid state absorption spectra of the employed matrices were acquired previously with a dual beam photospectrometer (UV-2102PC; Shimadzu, Duisburg, Germany) equipped with an integrating sphere (ISR-260; Shimadzu) [4].

Mass Spectrometry

The used mass spectrometer has been described in detail elsewhere [4, 41, 42]. In brief, it is a hybrid orthogonal extracting time-of-flight (oTOF) instrument equipped with a modified oMALDI2 ion source (AB SCIEX, Concord, Canada). Experiments were performed with a buffer gas pressure (N_2) in the region of ion generation of about 0.7 mbar. This value is at the upper range of pressures typically applied in oTOF-type MALDI instruments and, therefore, provides for efficient collisional cooling [41, 42]. In contrast, material expansion occurs into a high vacuum of typically 10^{-7} mbar in the more common axial-TOF MALDI mass spectrometers. The wavelength-tunable laser was a Nd:YAG laser-pumped frequency-doubled dye laser (FL-2001; Lambda Physik, Göttingen, Germany) with a line width of 2 nm, a pulse repetition rate of 10 Hz, and a pulse width of 6 ns. The following laser dyes (all from Radiant Dyes, Wermelskirchen, Germany) were used to provide a tuning range of 280–380 nm:

fluorescein 27 (emission wavelength range 560–580 nm), rhodamine 6G (580–590 nm), 10:1 (m/m) rhodamine B/rhodamine 100 mix (590–610 nm), DCM (610–650 nm), 4:1 (m/m) DCM/pyridine I mix (650–675 nm), pyridine I (675–720 nm), and styryl 8 (720–760 nm). The laser beam was coupled to the mass spectrometer via a 10 m-long fused silica fiber (SFM200/220Y; Fiberguide, Stirling, NJ, USA; core/clad diameter, 200/220 μm; numerical aperture, 0.12). The homogeneously illuminated end surface of the glass fiber was imaged 1:1 onto the sample plate using a telescope in order to produce a focal spot with near-flat top beam profile. Throughout the experimental wavelength range, at least up to 30 μJ/pulse could be supplied to the sample. Laser pulse energies were adjusted by means of a dielectric attenuator placed in the amplifier pump beam of the dye laser. This way, fine-attenuation of the pulse energy was achieved without affecting the output pulse energy stability. During acquisition of the mass spectra, the laser pulse energy was measured online by directing a fraction of the beam onto a calibrated pyroelectric detector. The pulse-to-pulse energy stability depended to some extent on the emission wavelength and was about 5%–15% throughout the investigated wavelength range. Focal spot sizes were determined at each wavelength setting using a custom-made device [43]. Wavelength dispersion effects were corrected as described previously by adjusting the positions of the fiber end surface and focusing lenses [4]. Owing to the angle of incidence of 30° the focal laser beam had an elliptical shape with half axis diameters (according to the D86 definition [43, 44]) of 205 ± 4 μm × 410 ± 8 μm; this corresponds to an irradiated area of 0.066 ± 0.002 mm^2.

Mass spectra were acquired using laser wavelengths between 280 and 377.5 nm, varied at a step size of 7.5 nm. For each wavelength, the mean laser pulse energy was first increased gradually until a stop rate of about 100 counts/s was recorded by the time-to-digital ion detector; roughly, this value marks the onset of sizable ion generation. Successively, fluences were increased in small increments until the 6- to 10-fold threshold value was reached. This way a maximum of 30–40 fluence data points were covered. Mass spectra were acquired by irradiating the samples with 300 laser pulses at each wavelength/fluence setting. During the 30 s-long data acquisition, the sample plate was continuously moved such that only the surface layers of the sample preparations were sampled to record one mass spectrum. Several identically prepared sample preparations were irradiated for recording data at one wavelength setting. Mass spectra were recorded using *tofmulti* software (courtesy of Victor Spicer and Werner Ens, University of Manitoba, Canada). The program was further modified in-house to allow for semi-automated signal intensity analyses. The minimum S/N for peak picking was set to 3.

MS Data Analysis

Ion signals corresponding to protonated monoisotopic peptide molecules were evaluated. Throughout this paper, the analyte ion signal intensity is defined as the sum of the peak area of the four peptide ion signals, derived over the full width at quarter maximum. Total ion counts (TIC) represent the sum of all counts generated by the ion detector in the *m/z* range between 150 and 3200. Electronic noise as well as residual ion counts for *m/z* values above 3200 were negligible for the chosen test system. Ions exhibiting *m/z* values below 150 were omitted in the calculation of the TIC because of the reduced transfer efficiency of the Q0 quadrupole of the hybrid oTOF instrument (the lower *m/z* limit of the quadrupole was set to 150 to provide high transmission efficiency for molecular peptide ions and fragments thereof).

Photoacoustic Analysis

The photoacoustic detection setup employed for recording the material ejection is shown in Figure 1. Sample plates were mounted at atmospheric pressure in a sealed quartz cuvette (a modified spare cuvette from the Lambda Physik dye laser). To allow manipulation without breaking the airtight seal of the cuvette, the sample plates were mounted on a magnet. A second magnet of opposite orientation, positioned on the outer side of the cuvette wall, held the sample plate in place. A micrometer screw was used to translate magnets and sample plate. A custom-made microscope with a 10 cm-long working distance (Walter Uhl technische Mikroskopie, Aßlar, Germany) served for observation of the samples during laser irradiation.

The laser beam was supplied using a similar optical setup as for the mass spectrometric measurements. In this case, the end surface of the optical fiber was imaged onto the sample by a single CaF_2-lens of 50 mm focal length at normal incidence. Dispersion effects arising from the multitude of wavelengths used were corrected by adjusting the positions of imaging lens and position of the SMA fiber mount. Two CaF_2 beam splitters of 2 mm thickness (transmission:reflection ratio, 98:2) were placed in the beam path to direct fractions of the light energy onto a calibrated pyroelectric detector (used for online monitoring of the pulse energies) and a linear diode array (15 μm resolution; EG&G, Reticon, Sunnydale, CA, USA), respectively. Both signals were registered with a digital oscilloscope (LC564A; LeCroy, Chestnut Ridge, NY, USA). Care was taken that the diode array detector was positioned at the same distance from the fiber end surface than the sample plate. Laser spot sizes were circular with an average diameter of 243 ± 25 μm corresponding to an area of 0.046 ± 0.01 mm^2 (D86 definition).

The pressure wave generated by the laser-material interaction was picked up with a capsule microphone (KE 4-211-1; Sennheiser, Wedemark-Wennebostel, Germany). The microphone was mounted ~10 mm above the "desorption site," thereby forming an angle of incidence α of ~90° for the impinging sound wavefront. Photoacoustic signals were pre-amplified using custom-built electronics and digitized with the oscilloscope. Exemplary transients gener-

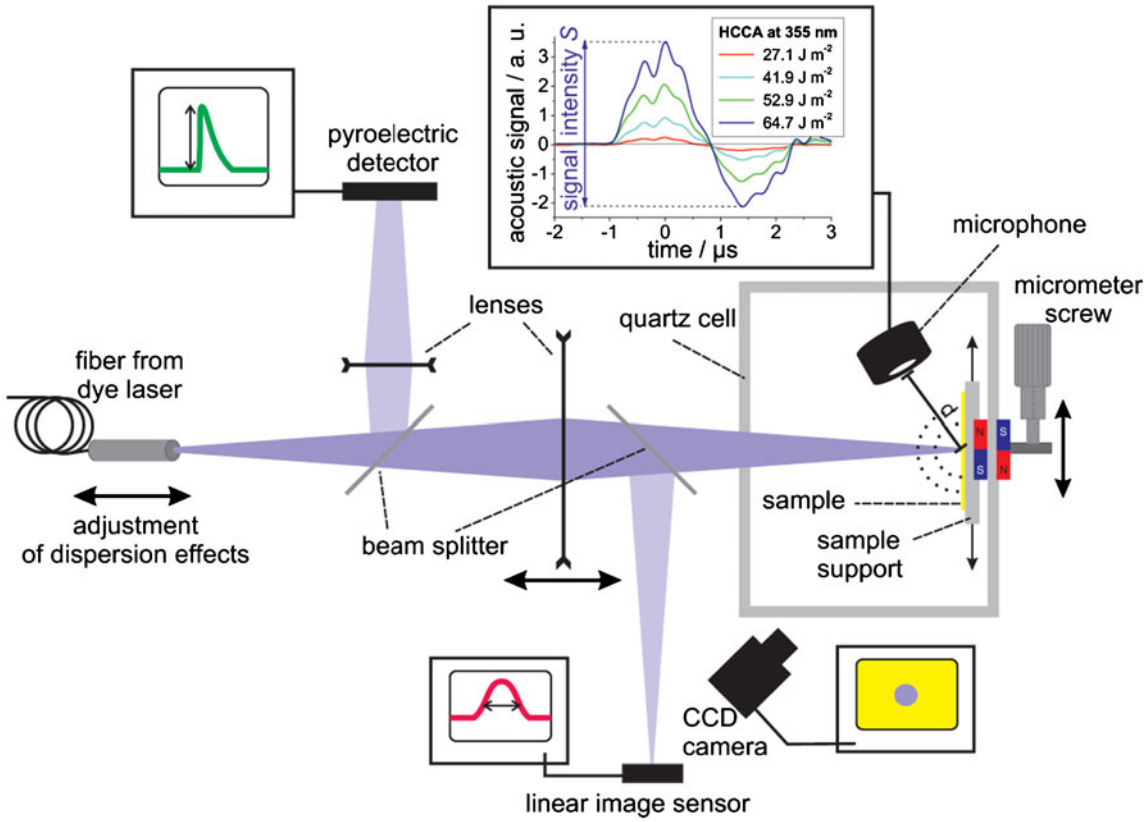

Figure 1. Layout of the photoacoustic setup used for recording the material ejection, including means for online measurement of laser pulse energy and laser spot size. The inset on top shows four acoustic transients generated upon excitation of the HCCA matrix with different fluences (each trace was averaged over 200 laser shots); the time axis was transposed such that the maximum of the first compressive amplitude forms the zero point

ated from the HCCA matrix at different fluences and at an excitation wavelength of 355 nm are displayed in the inset at the top of Figure 1. Data were recorded at the same wavelength settings as used in the MS experiments and by applying a similar multitude of different fluences. At each wavelength/fluence setting, 200 laser pulses were applied on different sample positions of the homogeneous sample preparations. The averaged photoacoustic signals were utilized for further data evaluation. The photoacoustic signal intensity S is defined as the amplitude of the first oscillation of the recorded sound wave (see inset in Figure 1). Because the signal is sizably affected by residual variations in laser spot size, a normalized photoacoustic signal S_n was derived for each wavelength setting by dividing S by the laser spot size A, determined using the diode array detector. A signal S_n exhibiting a signal-to-noise ratio (S/N) of 2 was defined as the lower "limit of detection." Starting at this value, the fluence was gradually increased until values exceeding the limit of detection by a maximal factor of ~5–10 were reached. Depending on the wavelength, up to 20–35 photoacoustic transients were recorded at different fluence values. Acquisition of photoacoustic data at higher fluences was not meaningful due to the excessive material ejection from the thin-layer sample preparations.

The transient photoacoustic signal is a superimposition of two components. Rapid heating of the air layer adjacent to the sample surface gives rise to a bipolar pressure wave. The amplitudes of this component are proportional to the applied laser pulse energy $c_T H$, where c_T is a thermoelastic factor and H the laser fluence [45]. In contrast, a contribution of a thermoelastic signal caused by the buildup and release of compressive stress within the excited matrix layers can be neglected for the shallow laser penetration depths between a few ten to some hundred nanometers and accordingly rapid stress relaxation times in the few 10 to ~200 ps-range [14].

Material ejection generates a second compressive component which, to first order, is proportional to the amount of material ejected [14, 17].

Contour Plots (Heat Maps)

Quasi-three-dimensional signal-intensity/wavelength/fluence surface plots ('heat maps') were generated using OriginPro 8.1 (OriginLab, Northampton, MA, USA). On the basis of the experimentally applied wavelength/fluence grid, the program interpolates the signal intensities. The heat maps provide a particular intuitive presentation of the complex data set. However, because of the step size of 7.5 nm for the

wavelengths reflecting a compromise between an experimentally accessible number of settings and a solid coverage of the MALDI-relevant wavelength range, and taking into account the different maximum fluences applied at the different wavelength points, boundary conditions are less well defined, and the contour plots should be interpreted with some care, especially in this fluence area. The same is true for cases of poorer statistics and/or larger data scattering. In particular, for calculation of the ion yields (to which two separately acquired data sets contribute) this may lead to an apparent "island effect."

Material Ejection (Desorption/Ablation) Models

Two models are most widely used to describe the material ejection under MALDI conditions. In the quasithermal model, molecular desorption is governed by the peak temperature reached in the uppermost matrix layers upon energy deposition. The model therefore predicts an exponential Arrhenius-type dependence of the material ejection N on the laser fluence H of the form

$$N \propto P e^{\frac{-Ea}{k_B(T_0+\eta H)}} \tag{1a}$$

where P is an empirical pre-exponential factor, E_A an activation energy needed to disintegrate the matrix crystal lattice, k_B the Boltzmann constant, T_0 the initial sample temperature, and η a factor describing the transformation of laser pulse energy into heat within a defined volume [3]. To first order η can be derived to

$$\eta = \frac{\alpha}{\rho c} \tag{2}$$

where ρ is the density of the solid state body and c its specific heat.

Neglecting possible non-equilibrium effects, η is, therefore, proportional to the absorption coefficient α. The quasithermal model has been found to describe the ejection of neutral particles, as probed by post-ionization [13, 46] and fast-flash imaging in dark-field geometry [14], in excellent agreement. Similar to the here applied photoacoustic approach, both methods, however, favor the detection of gaseous monomers over ejected clusters. Taking into account the additional thermoelastic component $c_T H$, the photoacoustic signal resulting from material ejection according the Equation 1a would be proportional to

$$S_n \propto c_T H + P e^{\frac{-Ea}{k_B(T_0+\eta H)}} \tag{1b}$$

The photoablation model takes into account possible overheating of the matrix material and the occurrence of a phase explosion when the deposited energy per volume exceeds a critical value [19, 37]. This results in the rapid ejection of a mixture of monomeric molecules and larger particles (clusters/droplets). For a laser beam with a flat-top beam profile, the overall ablated volume V_{abl} can be described as

$$V_{abl}(H) \propto \left[ln\left(\frac{H}{H_{thr}}\right)\right]^2 \tag{3a}$$

where H_{thr} denotes the threshold fluence for the process. The resulting photoacoustic signal can to first order be described as

$$S_n(H) \propto c_T F + \left[ln\left(\frac{H}{H_{thr}}\right)\right]^2 \tag{3b}$$

MD calculations simulating MALDI conditions put the fractions of ejected monomeric molecules versus clusters to about 0.6/0.4 [21]. Notably, if only the monomeric molecules are evaluated, their ejection is described steplessly by the quasithermal model both below and above H_{thr} [20].

Safety Hazard Note

The employed laser is of laser safety class 4. Protective goggles have to be worn when working with free beams of such lasers.

Results and Discussion

Material Ejection and Ion Signals as Function of Laser Wavelength and Fluence

Contour Plots Contour plots of the laser-induced material ejection from the four matrices, represented by the photoacoustic signal S_n, are displayed in Figure 2 as a function of wavelength and fluence. For "central" wavelengths around the peak absorption, the contour lines—in this context wavelength-fluence combinations that lead to equal amounts of desorbed material—exhibit essentially the same wavelength course as the mean optical penetration depth $\delta(\lambda) = \alpha(\lambda)^{-1}$, plotted in Figure 2 as solid white lines. Only at wavelengths of stronger diminished absorption a more notable deviation is eventually found. This finding shows that in the MALDI-relevant irradiation regime the material ejection is to a first order determined by the energy deposited into the upper matrix layers, $E_V = \alpha H$. Above the detection threshold, material ejection increases exponentially with fluence at all wavelengths (see detailed discussion below). In the low to moderate fluence range up to about 2–3 times the ion detection threshold, similar correlations are found for the total ion counts I_{TIC} (Figure 2b), which is assumed to be proportional to the sum of all gaseous ions generated in the MALDI process, while saturation effects become notable at higher fluence values (see discussion below). An even more complex picture is obtained for the molecular peptide ion signals I_A (Figure 2c). The fact that for

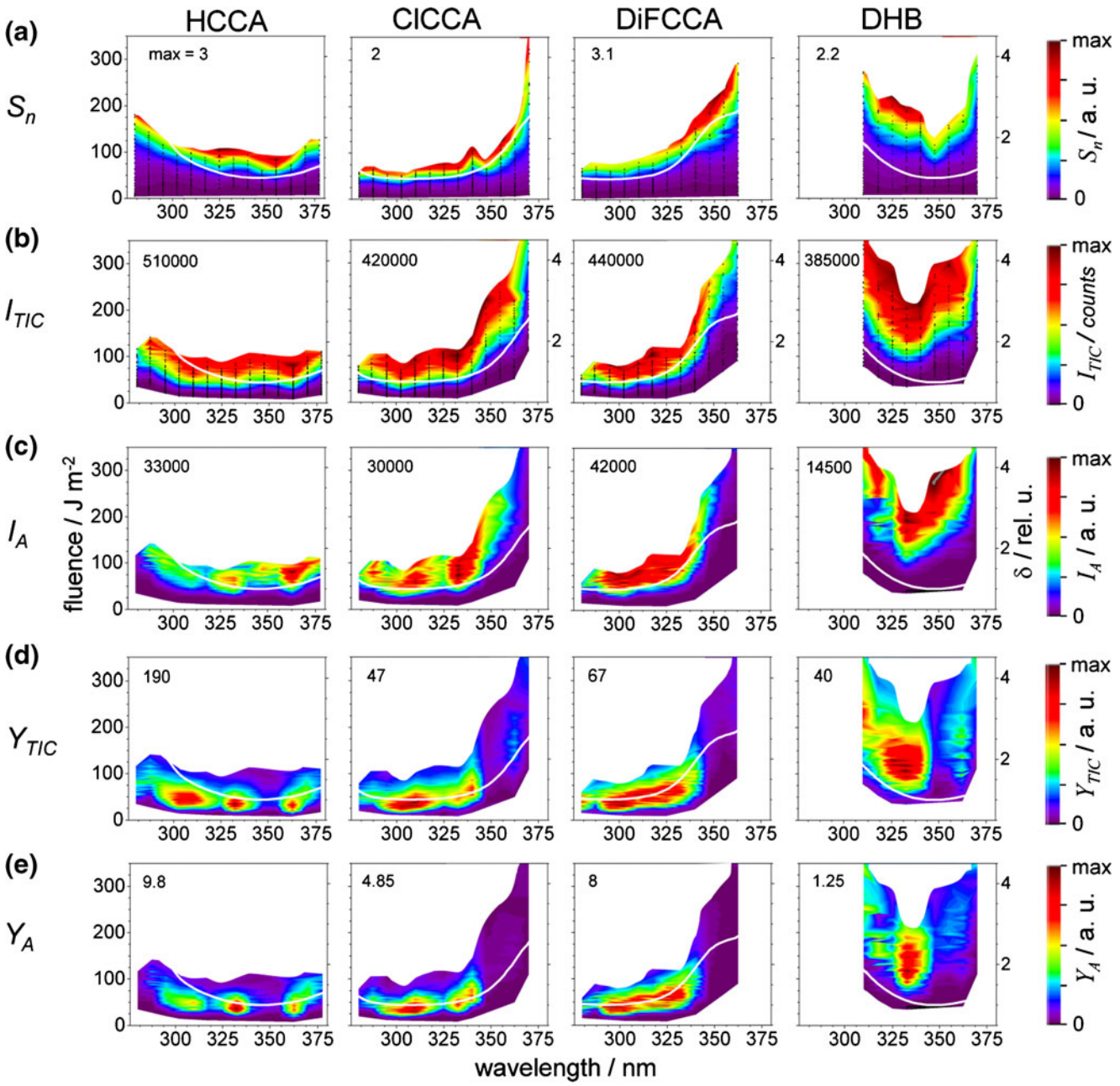

Figure 2. (**a**) Material ejection (represented by the normalized photoacoustic signal S_n, (**b**) total ion count I_{TIC}, (**c**) molecular peptide ion signal intensities I_A, (**d**) total ion yields Y_{TIC}, and (**e**) analyte ion yields Y_A as a function of matrix, laser wavelength, and laser fluence. The experimental wavelength/fluence data mesh underlying the generation of the heat maps is shown in **a** and **b**. Wavelength/fluence areas for which no meaningful data were derived are left blank, either because the experimentally available laser energy was not sufficient or because of excessive material ejection (for high fluences at wavelengths of high absorption). The heat maps for the MS data were normalized to their individual maxima to account for the different ion intensities obtained with the four compounds [4]. The individual maximum signal intensity values (in arb. units) are annotated in the upper left corner of the graphs. To account for the slight mismatch in fluence values used for acquiring MS- and photoacoustic data, respectively, for calculation of the ion yields the photoacoustic data were scaled using a best fit of the quasithermal model (Equation 1b) to the experimental data. The wavelength-dependent mean optical penetration depths $\delta = \alpha^{-1}$ of the matrices are plotted as white solid lines (in relative units because absolute absorption coefficients α cannot be derived from the solid state absorption spectra recorded in diffuse reflection geometry)

the three cinnamic acid derivatives generally higher signal intensities of the intact peptide ions are obtained toward the red shoulder of the absorption peak was attributed to an increased dissociation of the peptides at the higher photon

energies (blue shoulder) [4]. In contrast, for the "cooler" DHB matrix TIC and molecular peptide signals show similar wavelength dependences. Different to the CCA-derivatives, somewhat higher signal intensities even seem to be produced slightly toward the blue shoulder of the absorption peak (Figure 2c).

Neutral Material Ejection

To analyze the fluence dependence of material ejection and ion emission in more detail, signals generated from the DiFCCA matrix at three selected wavelengths corresponding to different optical absorptivities are displayed in Figure 3 in the form of signal intensity-fluence plots. Generally, the other three matrices produced similar data sets (not shown). In this type of presentation, it becomes especially obvious that neutral material ejection already commences at fluences substantially below the ion detection threshold, in line with previous studies [13, 14]. Generally, ion signals increase notably stronger than those for the material ejection [13, 14] before saturation effects set in at higher fluences.

For central wavelengths around the optical absorption peak, the material ejection as recorded by the photoacoustic method can for all four matrices be fitted with high precision by the quasithermal model of Equation 1b (solid lines in Figure 3a). Based on the available multitude of available wavelength/fluence combinations, similar best fit values for the activation energy E_a of ~0.3 ± 0.05 eV (~29 ± 5 kJ/mol) are derived for all four matrices, while the best fit values for η, which is describing the temperature increase in the excited matrix material upon laser energy deposition (Equation 2), are found to scale linearly with the experimental solid state absorption coefficients α. This finding is a strong evidence for the validity of the model assumption. Only at wavelengths of very low absorptivity (e.g., at 362.5 nm for the DiFCCA matrix), which are not MALDI-relevant because of the associated exceedingly low ion signals and ion yields (Figure 2a), somewhat stronger deviations of the model data may indicate a gradual transition towards different ejection mechanisms. As noted above, it must be left open at this stage whether a fraction of particles ejected in the form of clusters is indeed negligible for the central MALDI wavelength/fluence regime or whether the photoacoustic approach suppresses their detection. A cluster size-dependent bias might, therefore, influence the photoacoustic data. Attempts to fit the photoacoustic data with the phase explosion model of Equation 3b did in no case generate a meaningful fit for central wavelengths around the absorption peaks of the matrices.

Ion Emission

To some extent, the multidimensional data cube also allows unraveling details of the MALDI ionization mechanisms. For example, like for the neutral material ejection, the essential linearity between the contour lines for I_{TIC} and the wavelength-dependent mean penetration depth δ in the low- to intermediate fluence range (Figure 2b) implicates that the same number of ions (detected by the TOF-instrument) is generated at all central wavelengths, as long as the same energy per volume $E_V = \alpha H$ is deposited into the upper matrix layers. Ion probe measurements made by Puretzky and Geoheagan [47, 48] as well as computational simulations of Knochenmuss and Zhigilei [23] suggest that the detected MALDI ions generally stem from the leading edge of the expanding ejecta and, therefore, from the uppermost matrix crystal layers. Knochenmuss and Zhigilei attributed this finding to the low escape probability of ions (due to charge recombination) that are generated in the dense deeper material layers. These considerations could explain why for both TIC and molecular ion signals "saturation" sets in at fluences exceeding the 2- to 3-fold threshold values, although such saturation is not noted for the overall material ejection.

Frequently, an empirically power law of the form $I \propto H^m$, where m is a best fit factor, is used to semiquantitatively describe the increase of the MALDI ion intensities. This description accounts for the exponential increase of the ion signals with fluence but is neither reflecting physical mechanisms, which are strongly depending on a range of material and laser parameters, among others the wavelength and spot size, nor accounting for the flattening of the curves at higher fluences. As a consequence, a range of empirical exponents m have been determined in the literature spanning from m ~1 [35] to m > 10 [3, 29]. The ion saturation has been observed before but has not been considered in empirical descriptions [13, 34]. Making use of the extensive data set acquired in the current study, we found that a sigmoidal function of the form

$$I = \hat{I}\frac{(H + H_{thr})^m}{(H_k + H_{thr})^m + (H + H_{thr})^m} \quad (4)$$

provides an excellent description for the ion signal intensity–fluence relationship for both I_{TIC} and I_A (Figure 3b, c). The best fit parameter m was found to be not depend on the excitation wavelength but on the matrix ranging from 4.1 to 4.9 (±0.6) for the analyte ion intensity and 3.2 to 3.8 (±1) for the TIC. Compared with a simple power law, best fit values for m are smaller by about a factor of 0.75. This is due to the introduction of the additional factor (H_k+H_{thr}). Mathematically, H_k reflects the inflection point of the intensity–fluence relation. We will show below that the optimal analyte ion yields are obtained for fluences around H_k. Similarly, the ion detection threshold, H_k, scales approximately inversely linear with the absorption coefficient α.

Equation 4 includes the upper limit $\hat{I}$ which, in good approximation, is the experimental intensity maximum of

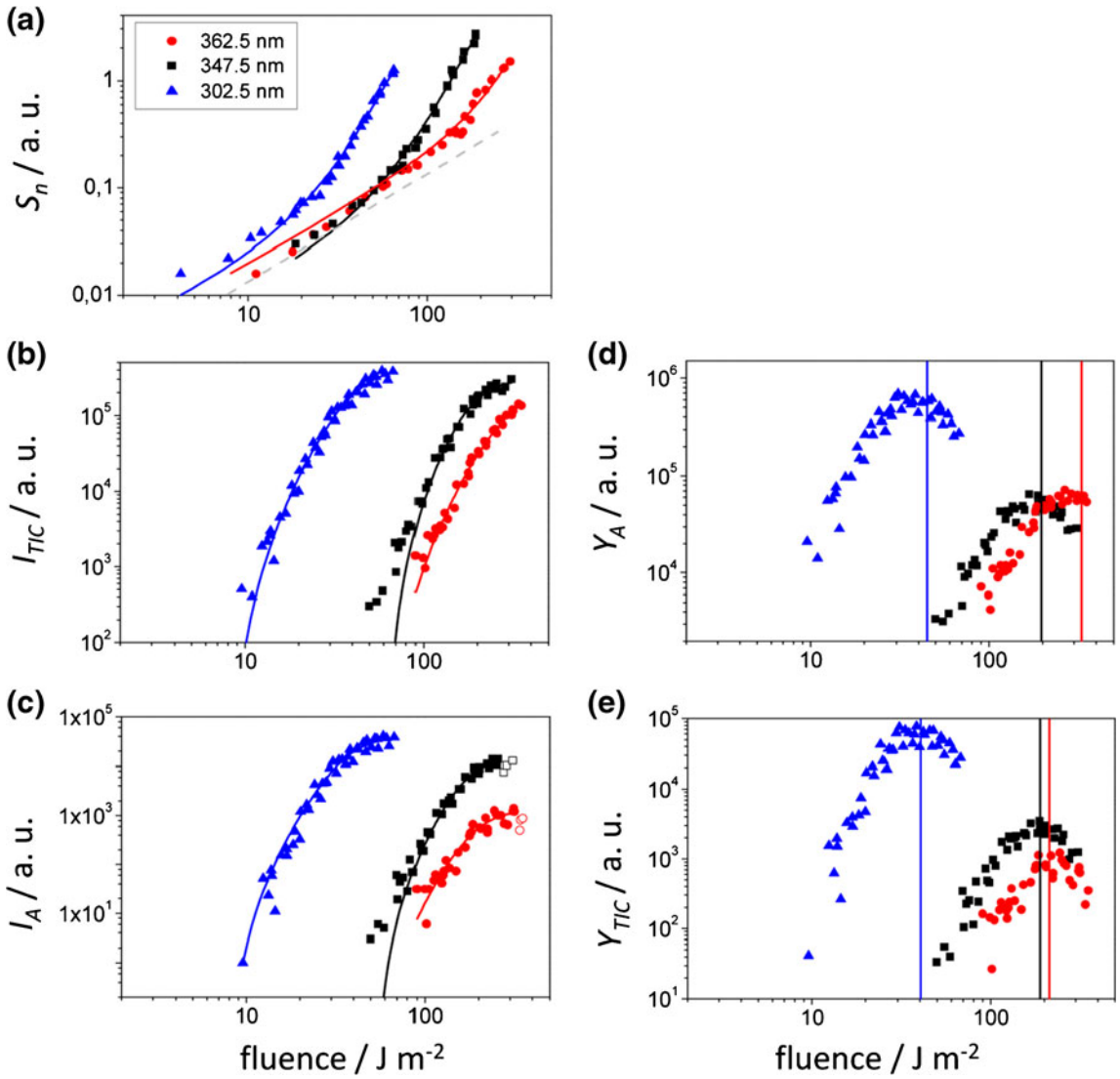

Figure 3. Fluence dependence of (**a**) the material ejection (represented by the photoacoustic signal S_n), (**b**) the total ion count I_{TIC}, (**c**) the molecular peptide ion signals I_A, (**d**) the total ion yield Y_{TIC}, and (**e**) the analyte ion yield Y_A at three selected wavelengths of different solid state absorptivities of the DiFCCA matrix ($\alpha_{302.5}$ = 1, $\alpha_{347.5}$ = 0.43, $\alpha_{362.5}$ = 0.38). Solid lines in (**a**) represent best fits of the quasithermal model of Equation 1b using an E_a of 0.3 ± 0.05 eV; the second fit parameter η scales linearly with the experimental absorption coefficient α(λ) (see text for details). The dashed line in (**a**) represent the linear part of Equation 1b, $c_T H$, resulting from heating of the air adjacent to the irradiated sample surface using the average value of c_T derived by fitting Equation 1b. Solid lines in (**b**) and (**c**) represent best fits of Equation 4 to the data (see text for further explanation); only data points represented by the solid circles were used for deriving the fits. The vertical lines in (**d**) and (**e**) denote the empirical factor H_k as derived by best fits of Equation 4 to the experimental data for I_{TIC} and I_A, respectively (see text for details). A linear plot for the data of (**a**)–(**c**) is provided in S-1 in Supplementary Material

either I_{TIC} or I_A. Owing to the additional wavelength-dependent fragmentation reactions to which the molecular ions are subjected, $\hat{I}_A$ shows a more complex dependence on the wavelength than $\hat{I}_{TIC}$. H_{thr} represents the fluence at which the sigmoidal fits intersect the abscissa and, therefore, a qualitative "threshold fluence" H_{thr} for the onset of a sizable ion production. Generally, values for H_{thr} are derived that differ only slightly from the experimental detection threshold. Note that the existence of a "real" threshold for the onset of MALDI ions has been discussed controversially in the literature [13, 32, 34]. Among other factors, the uncertainty arises from the steep laser fluence dependence.

Performing best fits of the sigmoidal function of Equation 4 to all measured data sets for the TIC and I_A provides wavelength-dependent values for $\hat{I}$ and H_{thr} that can serve to rapidly identify wavelength regions of maximum ion generation. These data are summarized in Figure 4.

As is already obvious from the contour plots (Figure 2c), for the CCA-derivatives the highest analyte signal intensities

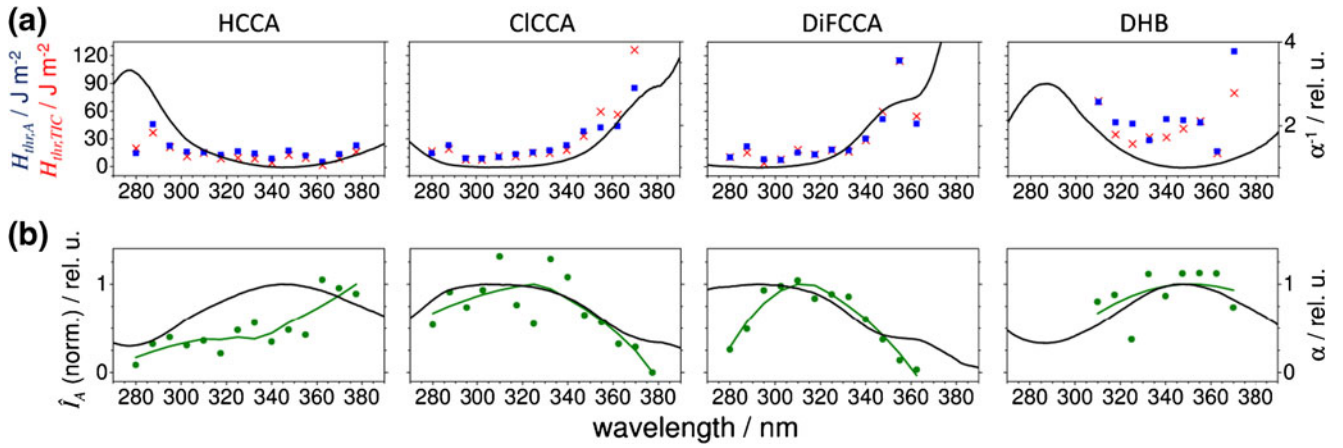

Figure 4. (**a**) Wavelength-dependent "threshold fluences $H_{thr,A}$" (blue squares) and $H_{thr,TIC}$ (red crosses) and (**b**) upper limits for the achievable analyte ion intensity $\hat{I}_A$ as derived from best fits of Equation 4 to the experimental data set for the four tested matrices. The mean penetration depth α^{-1} (**a**) and absorptivity α (**b**), respectively, of the matrices are displayed in black. The green lines in (**b**) represent the moving mean of four data points, intended to guide the eye. The maximum of the moving mean was used to normalize the data

$\hat{I}_A$ are found at wavelengths that are red-shifted from the absorption maxima by about 25–30 nm. In contrast, both $H_{thr,TIC}$ and $H_{thr,A}$ are closely following the absorption curve (Figure 4a). This indicates that the enhanced analyte fragmentation is a result of both high photon energy and laser fluence. For DHB, $\hat{I}_A$ peaks exactly around the optical absorptivity maximum.

Ion Yields

Total ion yields Y_{TIC} and analyte ion yields Y_A are derived (in relative units) by dividing I_{TIC} and I_A, respectively, by S_n (Figures 2d, e and 3d, e). For this purpose, S_n values were first "interpolated" for the exact fluence values at which I_{TIC} and I_A were recorded by utilizing best fits of Equation 1b to the experimental data. Note that absolute values cannot be derived because of the noncalibrated signals. Because of the intrinsic scatter of both data sets, ion yields obtained in this way show a larger experimental error that is also reflected by the artificial "island effect" in some of the heat maps—these should, hence, be interpreted with care. Within the given accuracy, it can, however, be concluded that highest total as well as the highest analyte ion yields are generally obtained at wavelengths that correspond to regions of highest matrix absorption. The red shift, which for the CCA-derivatives was notable between maximum ion signal intensity and maximum optical absorption, is somewhat reduced for the ion yield data. Note that the step size of 7.5 nm between the experimental wavelength points sets limits to an "exact determination" of the maximum. Nevertheless, as was noted before, optimal values for the "cooler" DHB are found in tendency toward shorter wavelengths than for the "hotter" CCA-derivatives. With respect to the laser fluence, values about a factor of 2–3 above the matrix- and wavelength-dependent ion detection thresholds provide an optimal sensitivity, while the use of both lower and higher fluences reduces the ion yields. Figure 3d and e show this fluence dependence for the total ion and the analyte ion yields at the example of the DiFCCA matrix. The vertical lines in the figure represent the inflection point H_k of the signal intensity/fluence graph as determined by best fits of Equation 4 to the ion signal data (see above). As apparent in the figure, H_k corresponds well with the fluence region of highest ion yield and can, therefore, be used as an indicator for optimal MALDI fluence conditions.

Conclusions

A MALDI event comprises intertwined processes of desorption and ionization, which in turn depend strongly on the material and irradiation parameters. Optimal results are generally only achieved if the best combination of matrix material, excitation, and instrumental parameters is employed for the specific analytical tasks at hand. In this regard, a sound knowledge about the MALDI processes and its dependence on the excitation wavelength and laser fluence can help to improve the analytical sensitivity and/or allow developing novel matrix compounds.

In this study, neutral material ejection and MS ion data were, for the first time, recorded in parallel for an extensive set of wavelength/fluence data points. A sensitive photoacoustic approach was developed that allows recording the molecular ejection under MALDI-typical fluence conditions. For wavelengths corresponding to a high optical absorption of the matrix, the generation of gaseous molecules by ns-laser pulses is governed by the quasithermal desorption model (i.e., by the peak temperature generated in the uppermost matrix layers). Because ion signals increase

with stronger fluence than the amount of ejected material, ion yields first increase when the fluence is raised above the ion detection threshold before a maximum is achieved about a factor of 2–3 above. Generally, optimal ion yields are obtained at excitation wavelengths that correspond to a high optical absorption of the matrix. However, fine features may arise from a reduced stability of the matrix and analyte compounds upon excitation with higher photon energies, as is observed for the CCA-derivatives.

Because of a reduced collisional cooling, such effects should be enhanced if ion emission takes place under high vacuum conditions. On the other hand, the presence of air in front of the sample, like in the photoacoustic experiments, should not influence the neutral material ejection significantly since the desorption process comprises a rapid phase transition from a dense solid state to an initialy dense gaseous one anyway.

The results illustrate that adjustment of wavelength and fluence settings according to the properties of the employed matrix offers a great potential for the optimization of MALDI-MS measurements. The findings of this study can, therefore, have substantial implications, in particular for applications in which only limited sample amounts are available and, hence, achieving a high ion yield is particularly crucial. One prominent example are MALDI MS imaging experiments where, in order to achieve a high lateral resolution and concomitantly sufficient sensitivity, a high fraction of analyte ions has to be generated from single small irradiated analyte-matrix voxels.

Acknowledgments

The authors thank Alexandre Loboda, Stefan Berkenkamp, Franz Hillenkamp, and Michael Karas for their support of this work. They thank Ulrich Röhling and Alexander Pirkl for technical assistance, Victor Spicer and Werner Ens (University of Manitoba) for providing the *tofmulti* program, Thorsten Deilmann for modifications of the program, and Richard Knochenmuss for helpful discussions. Financial support by the Deutsche Forschungsgemeinschaft (grants DR416/8-1 and DR416/9-1 to K.D. and JA2127/1-1 to T.W.J.) and the funds Innovative Medical Research of the Münster University Medical School (grant DR520805 to K.D.) is gratefully acknowledged.

References

1. Karas, M., Bachmann, D., Hillenkamp, F.: Influence of the wavelength in high-irradiance ultraviolet-laser desorption mass-spectrometry of organic-molecules. *Anal. Chem.* **57**, 2935–2939 (1985)
2. Beavis, R.C., Chaudhary, T., Chait, B.T.: α-Cyano-4-hydroxycinnamic acid as a matrix for matrix assisted laser desorption mass spectrometry. *Org. Mass Spectrom.* **27**, 156–158 (1992)
3. Dreisewerd, K.: The desorption process in MALDI. *Chem. Rev.* **103**, 395–425 (2003)
4. Soltwisch, J., Jaskolla, T.W., Hillenkamp, F., Karas, M., Dreisewerd, K.: Ion yields in UV-MALDI mass spectrometry as a function of excitation laser wavelength and optical and physico-chemical properties of classical and halogen-substituted MALDI matrixes. *Anal. Chem.* **84**, 6567–6576 (2012)
5. Wiegelmann, M., Soltwisch, J., Jaskolla, T.W., Dreisewerd, K. Matching the laser wavelength to the absorption properties of matrices increases the ion yield in UV-MALDI mass spectrometry. *Anal. Bioanal. Chem.* 2012, in press doi 10.1007/s00216-012-6478-5.
6. Horneffer, V., Dreisewerd, K., Lüdemann, H.C., Hillenkamp, F., Lage, M., Strupat, K.: Is the incorporation of analytes into matrix crystals a prerequisite for matrix-assisted laser desorption/ionization mass spectrometry? A study of five positional isomers of dihydroxybenzoic acid. *Int. J. Mass Spectrom.* **185**, 859–870 (1999)
7. Allwood, D.A., Dreyfus, R.W., Perera, I.K., Dyer, P.E.: UV optical absorption of matrices used for matrix-assisted laser desorption/ionization. *Rapid Commun. Mass Spectrom.* **10**, 1575–1578 (1996)
8. Wu, K.J., Steding, A., Becker, C.H.: Matrix-assisted laser desorption time-of-flight mass spectrometry of oligonucleotides using 3-hydroxypicolinic acid as an ultraviolet-sensitive matrix. *Rapid Commun. Mass Spectrom.* **7**, 142–146 (1992)
9. Chen, X.J., Carroll, J.A., Beavis, R.C.: Near-ultraviolet-induced matrix-assisted laser desorption/ionization as a function of wavelength. *J. Am. Soc. Mass Spectrom.* **9**, 885–891 (1998)
10. Qiao, H., Spicer, V., Ens, W.: The effect of laser profile, fluence, and spot size on sensitivity in orthogonal-injection matrix-assisted laser desorption/ionization time-of-flight mass spectrometry. *Rapid Commun. Mass Spectrom.* **22**, 2779–2790 (2008)
11. Mowry, C.D., Johnston, M.V.: Simultaneous detection of ions and neutrals produced by matrix-assisted laser desorption. *Rapid Commun. Mass Spectrom.* **7**, 569–575 (1993)
12. Puretzky, A.A., Geohegan, D.B., Hurst, G.B., Buchanan, M.V., Luk'yanchuk, B.S.: Imaging of vapor plumes produced by matrix-assisted laser desorption: a plume sharpening effect. *Phys. Rev. Lett.* **83**, 444–447 (1999)
13. Dreisewerd, K., Schürenberg, M., Karas, M., Hillenkamp, F.: Influence of the laser intensity and spot size on the desorption of molecules and ions in matrix-assisted laser-desorption ionization with a uniform beam profile. *Int. J. Mass Spectrom. Ion Process.* **141**, 127–148 (1995)
14. Rohlfing, A., Leisner, A., Hillenkamp, F., Dreisewerd, K.: Investigation of the desorption process in UV matrix-assisted laser desorption/ionization with a liquid 3-nitrobenzyl alcohol matrix by photoacoustic analysis, fast-flash imaging, and UV-laser post-ionization. *J. Phys. Chem. C* **114**, 5367–5381 (2010)
15. Quist, A., Huth-Fehre, T., Sundqvist, B.: Total yield measurements in matrix-assisted laser-desorption using a quartz-crystal microbalance. *Rapid Commun. Mass Spectrom.* **8**, 149–154 (1994)
16. Haulenbeek, J.R. Exploration of the effects of electrospray deposition spraying parameters and incident laser wavelength on matrix-assisted laser desorption ionization time-of-flight mass spectrometry; Ph.D. thesis, Drexel University, Philadelphia, PA, (2012)
17. Heise, T., Yeung, E.: Dynamics of Matrix-assisted laser-desorption as revealed by the associated acoustic-signal. *Anal. Chim. Acta* **299**, 377–385 (1995)
18. Rohlfing, A., Menzel, C., Kukreja, L.M., Hillenkamp, F., Dreisewerd, K.: Photoacoustic analysis of matrix-assisted laser desorption/ionization processes with pulsed infrared lasers. *J. Phys. Chem. B* **107**, 12275–12286 (2003)
19. Zhigilei, L.V., Garrison, B.J.: Microscopic mechanisms of laser ablation of organic solids in the thermal and stress confinement irradiation regimes. *J. Appl. Phys.* **88**, 1281–1298 (2000)
20. Zhigilei, L.V., Yingling, Y.G., Itina, T.E., Schoolcraft, T.A., Garrison, B.J.: Molecular dynamics simulations of matrix-assisted laser desorption—connections to experiment. *Int. J. Mass Spectrom.* **226**, 85–106 (2003)
21. Knochenmuss, R., Zhigilei, L.: What determines MALDI ion yields? A molecular dynamics study of ion loss mechanisms. *Anal. Bioanal. Chem.* **402**, 2511–2519 (2012)
22. Knochenmuss, R., Zhigilei, L.V.: Molecular dynamics model of ultraviolet matrix-assisted laser desorption/ionization including ionization processes. *J. Phys. Chem. B* **109**, 22947–22957 (2005)
23. Knochenmuss, R., Zhigilei, L.V.: Molecular dynamics simulations of MALDI: laser fluence and pulse width dependence of plume characteristics and consequences for matrix and analyte ionization. *J. Mass Spectrom.* **45**, 333–346 (2010)
24. Knochenmuss, R.: Ion formation mechanisms in UV-MALDI. *Analyst* **131**, 966–986 (2006)
25. Knochenmuss, R.: A quantitative model of ultraviolet matrix-assisted laser desorption/ionization. *J. Mass Spectrom.* **37**, 867–877 (2002)
26. Knochenmuss, R.: A quantitative model of ultraviolet matrix-assisted laser desorption/ionization including analyte ion generation. *Anal. Chem.* **75**, 2199–2207 (2003)

27. Knochenmuss, R.: A bipolar rate equation model of MALDI primary and secondary ionization processes, with application to positive/negative analyte ion ratios and suppression effects. *Int. J. Mass Spectrom.* **285**, 105–113 (2009)
28. Spengler, B., Bahr, U., Karas, M., Hillenkamp, F.: Postionization of laser-desorbed organic and inorganic-compounds in a time of flight mass-spectrometer. *Anal. Instrum.* **17**, 173–193 (1988)
29. Ens, W., Mao, Y., Mayer, F., Standing, K.G.: Properties of matrix-assisted laser desorption. measurements with a time-to-digital converter. *Rapid Commun. Mass Spectrom.* **5**, 117–123 (1991)
30. Demirev, P., Westman, A., Reimann, C., Hakansson, P., Barofsky, D., Sundqvist, B., Cheng, Y., Seibt, W., Siegbahn, K.: Matrix-assisted laser desorption with ultra-short laser-pulses. *Rapid Commun. Mass Spectrom.* **6**, 187–191 (1992)
31. Yau, P., Chan, T., Cullis, P., Colburn, A., Derrick, P.: Threshold fluences for production of positive and negative-ions in matrix-assisted laser desorption ionization using liquid and solid matrices. *Chem. Phys. Lett.* **202**, 93–100 (1993)
32. Ingendoh, A., Karas, M., Killenkamp, F., Giessmann, U.: Factors affecting the resolution in matrix-assisted laser-desorption ionization mass-spectrometry. *Int. J. Mass Spectrom. Ion Process.* **131**, 345–354 (1994)
33. Riahi, K., Bolbach, G., Brunot, A., Breton, F., Spiro, M., Blais, J.: Influence of laser focusing in matrix-assisted laser-desorption ionization. *Rapid Commun. Mass Spectrom.* **8**, 242–247 (1994)
34. Westmacott, G., Ens, W., Hillenkamp, F., Dreisewerd, K., Schürenberg, M.: The influence of laser fluence on ion yield in matrix-assisted laser desorption ionization mass spectrometry. *Int. J. Mass Spectrom.* **221**, 67–81 (2002)
35. Günther, S., Köstler, M., Schulz, O., Spengler, B.: Laser spot size and laser power dependence of ion formation in high resolution MALDI imaging. *Int. J. Mass Spectrom.* **294**, 7–15 (2010)
36. Allmen, M.V., Blatter, A.: Laser-beam interactions with materials: physical principles and applications. Springer, Berlin, Germany (1995)
37. Vogel, A., Venugopalan, V.: Mechanisms of pulsed laser ablation of biological tissues. *Chem. Rev.* **103**, 577–644 (2003)
38. Garrison, B.J., Srinivasan, R.: Microscopic model for the ablative photodecomposition of polymers by far-ultraviolet radiation (193 nm). *Appl. Phys. Lett.* **44**, 849–851 (1984)
39. Jaskolla, T.W., Lehmann, W.-D., Karas, M.: 4-Chloro-α-cyanocinnamic acid is an advanced, rationally designed MALDI matrix. *Proc. Natl. Acad. Sci. U. S. A.* **105**, 12200–12205 (2008)
40. Teuber, K., Schiller, J., Fuchs, B., Karas, M., Jaskolla, T.W.: Significant sensitivity improvements by matrix optimization: a MALDI-TOF mass spectrometric study of lipids from hen egg yolk. *Chem. Phys. Lipids* **163**, 552–560 (2010)
41. Loboda, A.V., Ackloo, S., Chernushevich, I.V.A.: High-performance matrix-assisted laser desorption/ionization orthogonal time-of-flight mass spectrometer with collisional cooling. *Rapid Commun. Mass Spectrom.* **17**, 2508–2516 (2003)
42. Soltwisch, J., Souady, J., Berkenkamp, S., Dreisewerd, K.: Effect of gas pressure and gas type on the fragmentation of peptide and oligosaccharide ions generated in an elevated pressure UV/IR-MALDI ion source coupled to an orthogonal time-of-flight mass spectrometer. *Anal. Chem.* **81**, 2921–2934 (2009)
43. Soltwisch, J., Dreisewerd, K.: An ultraviolet/infrared matrix-assisted laser desorption ionization sample stage integrating scanning knife-edge and slit devices for laser beam analysis. *Rapid Commun. Mass Spectrom.* **25**, 1266–1270 (2011)
44. Wright, D.: Beamwidths of a diffracted laser using four proposed methods. *Opt. Quantum Electron.* **24**, 1129–1135 (1992)
45. Rosencwaig, A., Gersho, A.: Theory of photoacoustic effect with solids. *J. Appl. Phys.* **47**, 64–69 (1976)
46. Dreisewerd, K., Schürenberg, M., Karas, M., Hillenkamp, F.: Matrix-assisted laser desorption/ionization with nitrogen lasers of different pulse widths. *Int. J. Mass Spectrom. Ion Process.* **154**, 171–178 (1996)
47. Puretzky, A.A., Geohegan, D.B.: Gas-phase diagnostics and LIF-imaging of 3-hydroxypicolinic acid MALDI-matrix plumes. *Chem. Phys. Lett.* **286**, 425–432 (1998)
48. Puretzky, A.A., Geohegan, D.B.: LIF imaging and gas-phase diagnostics of laser desorbed MALDI-matrix plumes. *Appl. Surf. Sci.* **127**, 248–254 (1998)